HHS Public Access

Author manuscript

Exp Eye Res. Author manuscript; available in PMC 2022 April 01.

Published in final edited form as:

Exp Eye Res. 2021 April ; 205: 108475. doi:10.1016/j.exer.2021.108475.

Histologic Validation of Optical Coherence Tomography-Based Three-Dimensional Morphometric Measurements of the Human Optic Nerve Head: Methodology and Preliminary Results

Massimo A. Fazio[1,2,3], **Stuart K Gardiner**[4], **Luigi Bruno**[5], **Meredith Hubbard**[6], **Gianfranco Bianco**[1], **Udayakumar Karuppanan**[1], **Jihee Kim**[2], **Mustapha El Hamdaoui**[1], **Rafael Grytz**[1], **J. Crawford Downs**[1], **Christopher A. Girkin**[1]

[1.]Department of Ophthalmology and Visual Sciences, University of Alabama at Birmingham; Birmingham, AL, United States.

[2.]Department of Biomedical Engineering, The University of Alabama at Birmingham; Birmingham, AL, United States.

[3.]The Viterbi Family Department of Ophthalmology, University of California, San Diego; San Diego, CA, United States.

[4.]Devers Eye Institute, Discoveries in Sight, Legacy Health; Portland, OR, United States.

[5.]Department of Mechanical, Energy and Management Engineering, University of Calabria; Rende CS, Italy.

[6.]Department of Neurobiology, The University of Alabama at Birmingham; Birmingham, AL, United States.

Abstract

Correspondence: Massimo A. Fazio, PhD, Associate Professor, Department of Ophthalmology and Visual Sciences, Department of Biomedical Engineering, University of Alabama at Birmingham, 1720 University Blvd., CEH 609, Birmingham, AL 35294, 205.934.8049, 205.934.3425 Fax, massimofazio@uabmc.edu.

Contributors:

Massimo A. Fazio: Conceptualization, Methodology, Software, Formal analysis, Investigation, Resources, Writing, Visualization, Supervision, Project administration, Funding acquisition;
Stuart K. Gardiner: Formal analysis, Data curation, Writing;
Luigi Bruno: Software, Visualization, Writing - Review & Editing;
Meredith Hubbard: Investigation, Data Curation, Writing - Review & Editing;
Gianfranco Bianco: Investigation, Methodology, Visualization, Writing - Review & Editing;
Udayakumar Karuppanan: Investigation, Data Curation, Writing - Review & Editing;
Jihee Kim: Software, Writing- Reviewing and Editing;
Mustapha El Hamdaoui: Investigation, Methodology;
Rafael Grytz: Investigation, Methodology, Writing - Review & Editing;
J. Crawford Downs: Investigation, Methodology, Writing - Review & Editing;
Christopher A. Girkin: Conceptualization, Methodology, Investigation, Resources, Writing, Supervision, Project administration, Funding acquisition.

Conflict of Interest: No conflicts of interest or financial relationships pertinent to this study exist for any of the authors. Hardware support was provided by Heidelberg Engineering, Inc. to MAF and CAG.

Purpose: To compare the three-dimensional (3D) morphology of the deep load-bearing structures of the human optic nerve head (ONH) as revealed in vivo by spectral domain optical coherence tomography (SDOCT) with ex vivo quantitative 3D histology.

Methods: SDOCT imaging of the ONH was performed in six eyes from three brain-dead organ donors on life-support equipment awaiting organ procurement (in vivo conditions). Following organ procurement (ex vivo conditions), the eyes were enucleated and underwent a pars plana vitrectomy followed by pressurization to physiologic IOP and immersion fixation. Ex vivo ONH morphology was obtained from high-fidelity episcopic fluorescent 3D reconstruction. Morphologic parameters of the observed ONH canal geometry and peripapillary choroid, as well as the shape, visibility and depth of the lamina cribrosa were compared between ex vivo and in vivo measurements using custom software to align, scale, and manually delineate the different regions of the ONH.

Results: There was significant correspondence between in vivo and ex vivo measurements of the depth and shape of the lamina cribrosa, along with the size and shape of Bruch's membrane opening (BMO) and anterior scleral canal opening (ASCO). Weaker correspondence was observed for choroidal thickness; as expected, a thinner choroid was seen ex vivo due to loss of blood volume upon enucleation (−79.9 %, $p<0.001$). In addition, the lamina was shallower (−32.3%, $p=0.0019$) and BMO was smaller ex vivo (−3.38%, $p=0.026$), suggesting post mortem shrinkage of the fixed tissue. On average, while highly variable, only 31% of the anterior laminar surface was visible in vivo with SDOCT ($p<0.001$).

Conclusions: Morphologic parameters by SDOCT imaging of the deep ONH showed promising correspondence to histology metrics. Small but significant shrinkage artifact, along with large effects of exsanguination of the choroid, was seen in the ex vivo reconstructions of fixed tissues that may impact the quantification of ex vivo histoarchitecture, and this should be considered when developing models and biomarkers based on ex vivo imaging of fixed tissue. Lack of visibly of most of the lamina surface in SDOCT images is an important limitation to metrics and biomarkers based on in vivo images of the ONH deep tissues.

1. Introduction

Spectral domain optical coherence tomography (SDOCT) has revolutionized clinical imaging of the optic nerve head (ONH) and retina, providing unprecedented visualization and quantification of the morphometry of these structures. Enhanced depth imaging (EDI) (Spaide et al., 2008), post-processing shadow-removal (Girard et al., 2011) and light attenuation compensation (Vermeer et al., 2013) algorithms have further improved visualization of the anterior surfaces of the deep ONH that are thought to be relevant to the remodeling of the load-bearing connective tissues seen with aging (Fazio et al., 2014a; Fazio et al., 2014b; Grytz et al., 2014a; Grytz et al., 2014b) and in the pathogenesis of glaucoma (sclera and lamina cribrosa) (Bellezza et al., 2003; Burgoyne, 2011; Burgoyne, 2015; Burgoyne and Downs, 2008; Burgoyne et al., 1995; Fazio et al., 2019) and myopia (Grytz et al., 2020b). However, even with these approaches to enhance visibility, the visualization of deep ONH structures remains limited due to obscuration from overlying tissue and signal attenuation (Kim et al., 2017). Moreover, there has been no histologic validation of structures segmented from SDOCT imaging of the deep ONH tissues. The need for

histologic validation of SDOCT of deep ONH structures is demonstrated from the efforts to histologically validate SDOCT-based morphology of the macula (Spaide and Curcio, 2011; Staurenghi et al., 2014), which has revealed that several of the reflectance bands seen in OCT have been incorrectly attributed to specific layers of the retina. This has had direct impact on clinical interpretation and retinal imaging research (Spaide and Curcio, 2011; Staurenghi et al., 2014) in a region that does not suffer from the shadowing and attenuation artifacts that instead limit visualization of deep ONH structures.

The present study employs a novel resource, the Living Eye Project (LEP) to enable the correlation of in vivo and ex vivo investigational methods in the living human eye (Fazio et al., 2018). LEP provides a unique platform in which ocular examination and imaging can be performed on brain-dead organ donors immediately prior to organ procurement in living conditions that are indistinguishable from in vivo conditions. After imaging in living conditions (referred as “in vivo” from here on), the same tissues can be immediately made available for ex vivo imaging and morphometric analyses immediately after organ procurement. For this study, we performed SDOCT imaging using a customized articulated positioning arm that allowed to image the organ donor’s eye prior to organ procurement. Following organ procurement, the same eyes were obtained and fixed at physiologic intraocular pressure (IOP). ONH tissues were processed and reconstructed using a high-resolution three-dimensional (3D) fluorescent episcopic reconstruction technique, as previously described (Girkin et al., 2017a). The purpose of this study is to determine how 3D custom metrics of the deep ONH tissue measured in vivo by SDOCT compared to ex vivo measures by high-definition autofluorescence histology.

2. Methods

2.1. Living Eye Project

LEP is a collaboration between the UAB Department of Ophthalmology and Visual Science, the Legacy of Hope Donor Recovery Center and Advancing Sight, formerly the Alabama Eye Bank. Legacy of Hope developed and opened the regional Donor Recovery Center at UAB in 2015 to provide centralized management for the workup and preparation of donors for organ and tissue transplant; they also provide a unique regulated platform for research in which examination, imaging, and biomechanical ocular testing can be performed in vivo (in living conditions) in ways not achievable in clinical patients. After in vivo testing and imaging, the same tissues are immediately made available for ex vivo imaging, testing, and analyses. Since the ocular tissues are available for morphometric and histologic study, along with cellular and molecular biologic approaches, this resource affords a unique opportunity to correlate in vivo ocular biomechanics with ex vivo testing. For this study, we performed SDOCT imaging in six eyes of three organ donors consented for research (age range [52,75] years old; all of European descent) maintained on life-support equipment while awaiting for organ procurement. Two donors had no ocular history while one had documented bilateral open angle glaucoma. All components of this study adhered to the Declaration of Helsinki and were approved by the UAB institutional review board and Legacy of Hope Research Review Board.

2.2. Inclusion and exclusion criteria

A certified tissue procurement technician conducted a structured interview with the next-of-kin to obtain the medical and ophthalmic history of donors consented for organ and tissue transplant and research. This interview includes specific questions regarding a history of glaucoma, macular degeneration or other retinal disease, prior ocular surgeries, and central nervous system (CNS) disease. Donors whose family reported a history of retinal, ONH or CNS disease other than glaucoma, or whose medical records revealed ocular pathology other than cataracts and/or cataract extraction, were excluded from the current study. The survey also assessed information regarding the identity and location of the donor's eye care provider and the consent to obtain this information was acquired. Any donor tissues for which the medical records were not available were excluded from this analysis. All the eyes were directly examined by a specialist in glaucoma and neuro-ophthalmology (CAG), including an indirect funduscopic examination. Only eyes with clear media, without any signs of agonal effects on the retina or ONH, and without any signs of ONH edema were included. In addition, any eyes with signs of retinal or ONH edema evident on initial baseline SDOCT imaging were excluded.

2.3. In vivo testing

2.3.1 Imaging by OCT.—The imaging protocol by SDOCT has been previously described in detail (Fazio et al., 2018). In brief, OCT imaging was performed with a second-generation spectral domain OCT equipped with a research software (Spectralis OCT2: Heidelberg Engineering Inc., Germany) and modified to mount the imaging head on a custom counterweighted support arm that allows for six-axis fine motion (Spectralis FLEX Module, Heidelberg Engineering Inc., Germany). With the organ donor in supine position, a baseline high-resolution 15° radial scan of the ONH was performed, which consisted of 24 B-scans made up of 768 A-scans each with 27 images averaged/B-scan. Axial scaling factor was 3.87μm for all the eyes and lateral scaling factor was 5.36μm on average; the actual transverse scaling for each eye was automatically estimated by the OCT control software based on an internal calibration model accounting for imaging distance and focus.(Grytz et al., 2020a) A total of 768x496x24 voxels were acquired per scan and arranged into a cylindrical coordinate system whose centroid was automatically located by the acquisition software based on the Bruch's membrane (BM) opening (BMO) point locations.

2.4. IOP control.

IOP was manometrically controlled via anterior chamber cannulation with a 27-gauge needle, connected to an adjustable phosphate-buffered saline reservoir. A digital manometer (XPi; Crystal Engineering, San Luis Obispo, CA) was placed in line with the needle to monitor input pressure, which was controlled by electronically-controlled electromagnetic valves. After canulation, IOP was set at 10mmHg for 2 minutes before acquisition of the OCT scan and maintained at the same pressure throughout the OCT scan. The cornea was lubricated with balanced salt solution and a plano hard contact lens was fitted on the cornea to maintain corneal hydration and avoid magnification changes during imaging caused by changes in corneal curvature.

2.5. Ex vivo testing

2.5.1. Tissue harvesting and preparation.—Donor eyes were removed via enucleation by an experienced eye bank technician. All eyes were obtained within six hours of enucleation, most of them within two hours. Following pars plana sclerotomies, two self-retaining retinal infusion cannulas, attached by intravenous tubing to custom pressurization device described below, were inserted into the vitreous cavity. An endoscopically guided vitrectomy was performed to ensure that no residual vitreous remained in the region of the inflow and outflow cannulas that could interfere with adequate maintenance of IOP.

2.5.2. Fixation at physiologic IOP.—All the enucleated eyes were immersion-fixed at an IOP of 10 mmHg. The inflow cannula was connected to a bottle of balanced salt solution (BSS) and a bottle containing a fixture solution of 2% glutaraldehyde and 1% paraformaldehyde in 0.1M phosphate-buffered saline solution. A three-way stopcock was used to change the inflow between the two bottles. First, the eyes were subjected to 10mmHg IOP using BSS. After 30 minutes, the eyes were immersed in the fixative solution and the inflow was changed from BSS to the fixative solution while maintaining IOP at 10mmHg. After six hours in fixative, the eyes were removed from the fixation chamber and the cannulas removed. The anterior segments were removed using scissors at the level of the pars plana and the posterior segments were submerged in 2% glutaraldehyde and 1% paraformaldehyde and left for another six hours. Eyes were then stored at 4°C in BSS until the episcopic autofluorescence imaging procedure described below.

2.5.3. Histologic 3D reconstruction by episcopic autofluorescence imaging. —Tissue preparation for episcopic autofluorescence imaging has been previously described in detail elsewhere (Girkin et al., 2017a).

Briefly, after the ONH and peripapillary sclera were separated from the posterior pole with an 8-mm-diameter trephine, specimens were photographed under a dissecting microscope, capturing the ONH and macula, and a small notch was cut in the superior edge of the trephined sclera for orientation. The trephined ONHs were then post-fixed in 5% glutaraldehyde for at least 48 hours to enhance tissue autofluorescence.

The trephined ONH tissues were dehydrated through a series of graded ethanol baths, and triple cleared in HPLC chloroform using a Sakura Tissue-Tek II automatic tissue processor (Ames Division, Miles Laboratories, Inc., Elkhart, IN). Tissues were then infiltrated with a mixture of 50ml chloroform and 0.25g Sudan IV dye (S4261, Sigma-Aldrich), first under 400mbar vacuum for 10 minutes, then at ambient atmospheric pressure for another 4 hours. The chloroform mixture was then pipetted off, and the specimens were infiltrated with a mixture of 25.0g stearic acid (S4751, Sigma-Aldrich) and 1.0g Sudan IV for 4 hours at 75°C under 400mbar vacuum. Specimens were then placed in paraffin embedding molds and infiltrated in the embedding mixture of 10.0g stearic acid, 1.6g Sudan IV, 72g paraffin (65°C melting point; 41663 Sigma-Aldrich), and 14.8g Vybar (Vybar 260, Candlewic, Inc) overnight at 75°C under 400mbar vacuum. Finally, the embedding mixture infiltration solution was pipetted off, and the molds were refilled with the embedding mixture a second time after paraffin block chucks were fitted to the molds, and allowed to cool into paraffin

tissue blocks. The embedding mixture has been optimized to block light across a broad spectrum, such that fluorescent imaging of the block face after microtome sectioning only captures those tissues exposed on the block face itself (Rosenthal et al., 2004; Weninger and Mohun, 2002). The ONH tissue was then digitally reconstructed using an automated episcopic fluorescence reconstruction technique as previously described (Girkin et al., 2017a). In brief, the system is based on a Leica RM-2265 microtome and Nikon AZ-100 microscope fitted with an Alta U-16M 16-megapixel grayscale camera, which have been modified to section the embedded ONH automatically under computer control, and capture a high-resolution fluorescent image of the block face after each 1.5-μm-thick section is taken. Each section image is aligned and stacked using a laser displacement sensor that detects the position of the tissue block at 200 nanometer precision while block face image is being acquired. This system captures the entire ONH and a ~2-mm-wide band of peripapillary sclera in its 6.25x6.25mm field of view, creating in a single 3D image volume of the ONH at an isotropic voxel resolution of 1.5x1.5x1.5μm. Digital 3D ONH reconstructions of each eye were approximately 15-35 gigabytes in size depending on the number of section images acquired and stacked.

2.6. Visualization and Delineation of the ONH scans

In vivo ONH OCT B-scans and ex vivo ONH digital reconstructions were both visualized in a custom software developed using the Visualization Toolkit; VTK, Clifton Park, NY (Multiview). The approach to 3D delineation with Multiview has been described in detail in prior publications (Girkin et al., 2017b; Yang et al., 2007). In brief, in 12 radial sections sequence of landmarks were manually placed so that their b-spline interpolation would overlay on the morphological surfaces of the ONH tissues, as shown in Figure 1. For the OCT scan volume, the 12 sections were taken one every other for the 24 imaged B-scans. For the episcopic autofluorescence imaging volume, 12 sections were taken by numerically sample the raster imaging volume with the rotation axes placed in the center of the ONH. In the histologic fluorescent 3D reconstructions, the observer manually delineated eight anatomic surfaces (Figure 1). Only the three surfaces were also delineated within each section of the OCT B-scan images and used for this study, as shown in Figure 1. The three anatomical surfaces delineated in the OCT were: BM, anterior scleral surface (Figure 2), and anterior lamina cribrosa surface (ALCS; see Figure 3). BMO and anterior scleral surface canal opening (ASCO) were computed by selecting the innermost point of their corresponsive surfaces at the neural canal. The full set of manually delineated landmarks were then used to generate a 3D point cloud representing the ONH anatomy from which the morphometric quantifications were obtained.

2.7. 3D quantification of the ONH morphology

The custom 3D quantification method of the ONH morphology relies exclusively on the 3D coordinates of the manually delineated landmarks. From this point forward, we will refer to the 3D anatomical landmarks obtained from either in vivo OCT or ex vivo fluorescent 3D reconstructions interchangeably.

2.7.1. BMO and ASCO morphology reference planes.—

For the 3D points representing the BMO points, a best-fit plane was obtained and used as a reference plane, as

described previously (Girkin et al., 2017b; Johnstone et al., 2014). The BMO points were then projected into the reference plane and fitted with a 2D ellipse, as shown in Figure 2A. Minor, maximum, and area of such ellipse were used as metrics to characterize the ONH disk morphology. An identical approach was used to fit the ASCO points (Figure 2B).

2.7.2. Choroidal thickness.—A cylinder of 1500 micrometers radius, with its axis passing through the BMO center in the direction normal to the BMO reference plane, was used to define a 250-μm-wide anulus where the distance between BM and the anterior scleral surface was averaged into a single value for choroidal thickness (Johnstone et al., 2014). The 3D representation of the BM and the anterior scleral surface points belonging to the anulus are highlighted in Figure 2C.

2.7.3. BM and scleral reference planes.—The BM points falling within the anulus region described in the paragraph above (Fig. 2C) were used to fit a third reference plane, which defines the BM reference plane. Metrics based on this BM reference plane have been of some interest to other authors based on the fact that the peripheral BM surface is generally flatter than the BM closer to the ONH. Hence, one could argue that a reference plane based on more peripheral landmarks would vary less across individuals. Similarly, 3D points belonging to the anterior scleral surface and in the anulus region were used to fit a scleral reference plane. Similar reference planes have been used in prior studies because the height of this plane is less affected by choroidal thickness, which has been shown to change with age, race, longer axial length, ONH area, and gender (Johnstone et al., 2014; Yang et al., 2019).

2.7.4. ALCS fitting surface and shape.—3D points defining the ALCS (Figure 3) were fitted by a 3D paraboloid with functional form:

$$\boldsymbol{ALCS}(\boldsymbol{x},\boldsymbol{y}) = ax^2 + bx + cxy + dy^2 + e \qquad \text{eq.1}$$

with, a, b, c, d and e, representing linear fitting parameters.

The shape of the ALCS was defined by curvature metrics as follows: a first metric was the largest (ε_I) eigenvalue of the Hessian matrix (second order derivatives of the functional form in eq. 1) and defined ALCS maximum curvature; a second metric for ALCS curvature was the lamina cribrosa curvature index (LCCI) defined by Kim et al. (Lee et al., 2017) which represents the distance between the central lamina and a plane fitting the BMO points projected onto the ALCS; a third metric for ALCS curvature was the global shape index (GSI) as previously defined (Sharma et al., 2018; Thakku et al., 2015) and was computed from the Hessian eigenvalues as 2π*ArcTan(($\varepsilon_I + \varepsilon_{II}$)/ ($\varepsilon_I - \varepsilon_{II}$)).

2.7.5. ALCS Depth.—The distance between the ALCS and the four reference planes was computed representing the ALCS depth from the 1) BMO, 2) ASCO, 3) BM, and 4) scleral reference planes. For each reference plane, ALCS depth was computed as the average distance (numerical integration) between a central region of the ALCS and the given reference plane. The central region of the ALCS was identified by the intersection between

the ALCS and a cylinder 500 mm in radius, perpendicular to the given reference plane, and passing for the corresponding centroid, as shown in Figure 3.

2.7.6. ALCS Visibility.—While the entirety of the ALCS is visible in histologic fluorescent 3D reconstructions(Girkin et al., 2017a) while only portions of the ALCS are visible in the in vivo OCT scans.(Girard et al., 2015b) We quantified the differences in ALCS visibility between in vivo and ex vivo approaches by computing the area of a triangular mesh (Delaunay's method) connecting the manually delineated ALCS points as projected into the BM reference plane.

2.8. Statistical analysis

Linear mixed effect models, with random effects for each subject that account for correlation between fellow eyes were used to compute the coefficients of determination (Zhang, 2017) (R^2) and corresponding p-values for the agreement between in vivo and ex vivo measurements for each of the computed morphological parameters. Bland-Altman plots and corresponding 95% confidence interval (CI) limits of agreement (LoA) intervals (Sedgwick, 2013) adjusted for clustering of the two eyes per individual (Bland and Altman, 2007) were computed to test for disagreement between the in vivo and ex vivo measurements. In accordance with the Bland-Altman metric for disagreement, the relative difference between in vivo and ex vivo metrics were computed as $\frac{\text{in vivo} - \text{ex vivo}}{(\text{in vivo} + \text{ex vivo}) / 2}$ for each of the computed morphological parameters; note that the ratio represents the quantities reported in the vertical (numerator) and horizontal (denominator) axes of a Bland-Altman plot.

3. Results

The correlation parameters for in vivo and ex vivo measurements and the LoA for the relative difference between in vivo and ex vivo metrics are summarized in Table 1. Estimated mean and corresponding p-values for each LoA are also reported in Table 1. Bland-Altman plots comparing the difference vs. the average of the in vivo and ex vivo measurements are shown in Fig. 5, where the continuous horizontal line represents the mean value, calculated by averaging the results of all six eyes, and the dashed lines show the upper and lower LoA. Each data point in the Bland-Altman plots is labeled "N" for normal eyes and "G" for glaucoma eyes followed by a number indicating the subject ID.

3.1. BMO and ASCO.

In vivo vs. ex vivo measurements for the BMO major axis, minor axis and area were tightly correlated (major axis: R^2=0.779, p<0.001; minor axis: R^2=0.737, p<0.001; area: R^2=0.62, p<0.001), as shown in Tab. 1.

LoA for the relative difference between the in vivo and ex vivo parameters showed a narrow band of agreement, with the range showing a slightly larger major axis in the in vivo measurements [−5.09, 11.6] %, as shown in Fig. 5. LoA are also shown for the BMO minor axes [−9.22, 11.3] %, and area [−8.65, 17.4] %.

Similar results were attained for the ASCO major axis, minor axis and area (major axis: R^2=0.834, p<0.001; minor axis: R^2=0.762, p<0.001; area: R^2=0.798, p<0.001). LoA for the relative difference between in vivo and ex vivo measures were [−6.71, 13.2] % for the ASCO major axes, [−10.4, 14.5] % for the ASCO minor axes, and [−12.4, 24.0.] % for the ASCO area. Bland-Altman plots and LoA for the ASCO parameters are shown in Figure 6.

3.2. Choroidal thickness.

Choroidal thickness showed poor correlation between in vivo and ex vivo measures and was not significant (R^2=0.201, p=0.036). LoA of the relative difference between in vivo and ex vivo showed a thicker choroid in the in vivo measures [34.0%, 128.0%], as one would expect considering the lack of choroidal blood perfusion in ex vivo reconstructions. Bland-Altman plot of the agreement is shown in Fig. 7, left plot.

3.3 ALCS visible area.

Visible area of the ALCS showed high correlation between in vivo and ex vivo measures (R^2=0.454, p<0.001). LoA of the in vivo vs. ex vivo relative difference showed visibility of the ALCS to be between −98% and −41% smaller compared to ex vivo measures (95% CI, p<0.001). Bland-Altman plot of the agreement shown in Fig. 7, right plot.

3.4. ALCS depth.

In vivo and ex vivo average distance between the ALCS surface and the BMO, BM, ASCO, and scleral reference planes demonstrates good correlation (from BMO: R^2=0.716, p<0.001; from BM: R^2=0.721, p<0.001; from ASCO: R^2=0.843, p<0.001; from sclera: R^2=0.83, p<0.001). LoA of the relative differences showed a deeper (posteriorly displaced) ALCS in vivo irrespective from the chosen reference plane (from BMO: [14.9, 54.6] %; from BM: [15.0, 53.0] %; from ASCO: [13.0, 50.2] %; from sclera [12.3, 49.5] %; Figure 8).

3.5. ALCS curvature and shape.

In vivo vs. ex vivo ALCS curvature metrics were highly correlated (R^2=0.835, p<0.001; LCCI: R^2=0. 706, p<0.001; GSI: R^2=0.596, p<0.001; Table1). Quantification of the in vivo vs. ex vivo relative differences showed very broad ranges of the LoA with only LCCI showing moderate significance, as reported in Table 1. Figure 9 shows the LoA of all the ALCS curvature parameters.

4. Discussion

This study reports the first direct comparison between the 3D morphology of deep ONH structures in the human eye obtained in vivo using optical coherence tomography and ex vivo histology quantified by episcopic autoflorescent 3D reconstructions. Even with a small number of observations, we demonstrated strong correspondence between in vivo and ex vivo measurements of the depth and shape of the lamina cribrosa along with size and shape of the ONH disk (BMO and ASCO). This study provides the first histologic validation of these deep optic nerve structures in humans as visible in vivo by SDOCT which are potential biomarkers of ONH remodeling in glaucoma, and are important parameters in modeling the biomechanical behavior of the ONH (Sigal et al., 2005; Sigal et al., 2014).

Prior postmortem studies that have defined the histoarchitecture of the human ONH have generally used eyes immersion fixed in the absence of inflation pressure (mimicking IOP) which greatly distorts the anatomy of these load-bearing tissues. In order to appropriately compare the in vivo and ex vivo morphometric parameters, we fixed the eyes while maintaining a similar IOP at which the OCT imaging was obtained (10mmHg), and we quantified the 3D histoarchitecture of the ONH using custom software that affords identical parameterization of the in vivo and ex vivo manually delineated images.

While OCT imaging is widely used clinically, few reports have explored comparisons between in vivo OCT-based measurements with ex vivo histology. These reports have been limited to the macular region and have been used to validate and redefine reflectance bands important for clinical image interpretation and retina research, and all use 2D techniques that are subject to angular artifact (Curcio et al., 2011). Similarly, the deep structures of the ONH are emerging as promising biomarkers in the detection of glaucoma and the prediction and detection of progressive disease (Bellezza et al., 2000; Burgoyne and Downs, 2008; Burgoyne et al., 2005; Downs et al., 2008; Fortune et al., 2013). Validating the degree to which in vivo imaging of deep ONH structures reflect the histoarchitecture of these load-bearing tissues is made more difficult by decreased visualization in this region compared to the macula. In contrast to the conserved ordered arrangement of the retinal reflectance bands in the macular region, the ex vivo/in vivo comparison of the ONH region is more challenging and less consistent due to the complex three-dimensional geometries of the laminar and scleral surfaces. An unbiased comparison across studies requires a detailed and accurately oriented three-dimensional segmentation with consistent alignment across approaches. Our study employed previously used manual segmentation and orientation approaches which, while laborious, affords the use of the same custom software and 3D quantification approach with both histologic and OCT-based images and volumes.

While this histologic validation is encouraging, there were several notable differences between ex vivo and in vivo histologic measurements. Though the difference in means was only significant for BMO major axis, the predominantly positive values of the LoA ranges for both BMO and ASCO area and major axis is suggestive of a smaller neural canal in the ex vivo conditions, which is possibly due to tissue shrinkage occurring after fixation. These differences are likely to impact models of ONH biomechanical behavior and morphologic biomarkers that are derived from ex vivo histology and should be accounted for when using these approaches. In addition, some of the observed difference may have be caused by optical distortions of the OCT images. Our data is insufficient to distinguish differences that are caused by optical distortions of the in vivo imaging or shrinkage of the ex vivo data. Dedicated investigations of the OCT optical distortion by injection in the retina of targets of known dimension (glass beads of known diameter), as proposed by Grytz et al. (Grytz et al., 2020a), are warranted.

A significant portion of the ALCS was obscured by overlying sclera, neuro-retinal and/or vascular tissue in the OCT images of all eyes. Visibility of the lamina cribrosa remains limited in OCT images, even when light-attenuation compensation algorithms and EDI imaging are employed (Girard et al., 2011; Mari et al., 2013; Vermeer et al., 2013). ALCS visibility was about 70% lower in vivo compared to ex vivo conditions where the entire

lamina is visible (69.2%, p<0.001; LoA [−98.5, −40.6], 95% CI; Table 1). A study on primates looking at ALCS visibility before and after exsanguination (Tran et al., 2018) reported a 35% lower visibility of ALCS in vivo; the higher magnitude of change seen in our study is likely imputable to the overall lower visibility of the ALCS in humans compared to primates. Small visibility of ALCS in vivo may limit the ability of models based on in vivo images to fully capture the morphology of the lamina cribrosa (Belghith et al., 2017; Girkin et al., 2019; Girkin et al., 2017c) and its biomechanical behavior (Fazio et al., 2016).

As expected, there was poor correlation in choroidal thickness measured in vivo and ex vivo, with a thinner choroid found in the ex vivo metrics likely due to exsanguination of choroidal blood volume. This artifact may propagate to any metric that involves measurements across the choroid. Consequently, the thinner choroid seen in the ex vivo data may have also resulted in a shallower lamina cribrosa depth measured ex vivo using the BMO- or BM-based reference planes. These reference planes are anterior to the choroid and would migrate posteriorly with exsanguination of the choroid following organ recovery. A similar effect has been reported during age-related thinning of the choroid.(Rhodes et al., 2015) However, even when ALCSD was measured using the scleral or ASCO reference plane, this difference (ASCO: 95% CI for LoA: 13.0 to 50.2 %, sclera: 95% CI for LoA: 12.3 to 49.5 %) was only slightly reduced and large differences still persisted indicating that additional factors such as tissue shrinkage may be the primary cause of these differences between our ex vivo vs in vivo data. It is also possible that the lack of retrolaminar pressure may have added some artifact to the position of ALSCD. While all donor eyes had no signs of optic nerve edema in vivo, we are not able to precisely estimate retrolaminar pressure in vivo or control retrolaminar pressure during fixation. This would likely artifactually increase the translaminar pressure gradient applied to the ONH during fixation. However, it would be expected that this reduced opposition force to IOP would result in greater posterior deformation in the ex vivo state resulting in a deeper ALSCD ex vivo measurement, so this effect is likely overshadowed by the effects of tissue shrinkage. Ultimately, sclera curvature, a factor not accounted for in this study, may also affect ALCSD.(Wang et al., 2019)

This study has several limitations. Foremost is the limited number of eyes available for direct comparison in vivo and ex vivo. While it is an encouraging observation that correspondence in limits of agreement of several key characteristics was similar across all the observed eyes, proper estimates of the population averages cannot be achieved. The unique resource developed for this study will provide a platform to obtain these data in the future as our studies expand. Encouragingly, the histologic parameters for the normal eyes in this study were within the range seen in our prior study quantifying the 3D ONH morphology in a much larger set of normal donors.(Girkin et al., 2017a) The shallower lamina for the average set of eyes seen in Girkin et al.(Girkin et al., 2017a) was expected considering that in that study all the lamina delineation points were there used while in this study the central points are only included in the computation of laminar depth. No prior work has evaluated the 3D histomorphology in glaucomatous human eyes with an episcopic approach. The OCT-derived parameters all fell within the range of prior work in normal (Rhodes et al., 2014) and glaucomatous eyes (Belghith et al., 2017). Secondly, as mentioned before, lack of retrolaminar pressure applied during ex vivo fixation also may introduce some artifacts in laminar and peripapillary scleral position (Fazio et al., 2018). However, it is

likely overshadowed by post-fixation tissues shrinkage as mentioned above. Furthermore, cause-of-death varied across subjects and some underling pathologies could possibly affect appearance of the ONH. However, a unique aspect of this approach is the ability to confirm normality (or pathology) of the donor tissue in its in vivo conditions. Eyes were only included if the optic nerve and retina appeared normal based on screening indirect funduscopic examination performed by a subspecialist in glaucoma and neuroophthalmology (CAG) and no evident signs of optic nerve or retinal edema were present either on fundus examination or baseline imaging. Lastly, ALCS visibility in vivo is partially device-dependent, as shown by Girard et al. (Girard et al., 2015a); hence, the reported metrics for ALCS visibility can possibly differ would the in vivo imaging be performed with a device different from the Spectralis OCT2 (Heidelberg Engineering Inc., Germany) used in this study.

5. Conclusions

3D quantitative metrics based on SDOCT imaging of the deep optic nerve tissues show promising correspondence to ex vivo metrics based on histology imaging. Small but significant differences (likely shrinkage) was seen in histology 3D reconstructions of fixed tissues; this may impact biomechanical models of the ONH and morphologic biomarkers that were derived from ex vivo histology. While it is promising that correspondence was seen across in vivo and ex vivo imaging, further work with a larger number of participating donors is needed to more clearly define the relationships between morphology of the deep optic nerve head as imaged in vivo by SDOCT and ex vivo histology.

Acknowledgements

This work was funded by: The National Eye Institute, R01 EY028284 (CAG, MAF), R01EY026574 (MAF, CAG), R01EY027759 (RG), P30EY003039 (CAG, MAF, JCD, RG); EyeSight Foundation of Alabama (MAF, JCD, CAG, RGG); Research to Prevent Blindness (MAF, JCD, CAG)

Financial Support:

National Eye Institute: R01EY028284 (CAG, MAF), R01EY026574 (MAF, CAG), R01EY027759 (RG), R01EY030096 (MH), P30EY003039 (CAG, MAF, JCD, RG); EyeSight Foundation of Alabama (MAF, JCD, CAG, RG); Research to Prevent Blindness(MAF, JCD, CAG)

Abbreviations:

SDOCT	Spectral domain optical coherence tomography
ONH	optic nerve head
LEP	Living Eye Project
3D	three-dimensional
IOP	intraocular pressure
CNS	central nervous system
BSS	balanced salt solution

BM	Bruch's membrane
BMO	Bruch's membrane opening
ASCO	anterior scleral canal opening
ALCS	anterior lamina cribrosa surface

References

Belghith A, Girkin CA, Weinreb RN, Medeiros F, Bowd C, Liebmann JM, Fazio MA, Zangwill LM, 2017. The African Descent and Glaucoma Evaluation Study (ADAGES): Racial differences in the posterior displacement of the anterior laminar cribrosa surface depth. Investigative Ophthalmology & Visual Science 58, 4015–4015. [PubMed: 28800648]

Bellezza AJ, Hart RT, Burgoyne CF, 2000. The optic nerve head as a biomechanical structure: initial finite element modeling. Invest Ophthalmol Vis Sci 41, 2991–3000. [PubMed: 10967056]

Bellezza AJ, Rintalan CJ, Thompson HW, Downs JC, Hart RT, Burgoyne CF, 2003. Deformation of the lamina cribrosa and anterior scleral canal wall in early experimental glaucoma. Invest Ophthalmol Vis Sci 44, 623–637. [PubMed: 12556392]

Bland JM, Altman DG, 2007. Agreement Between Methods of Measurement with Multiple Observations Per Individual. Journal of Biopharmaceutical Statistics 17, 571–582. [PubMed: 17613642]

Burgoyne CF, 2011. A biomechanical paradigm for axonal insult within the optic nerve head in aging and glaucoma. Experimental Eye Research 93, 120–132. [PubMed: 20849846]

Burgoyne CF, 2015. The non-human primate experimental glaucoma model. Exp Eye Res 141, 57–73. [PubMed: 26070984]

Burgoyne CF, Downs JC, 2008. Premise and prediction-how optic nerve head biomechanics underlies the susceptibility and clinical behavior of the aged optic nerve head. Journal of glaucoma 17, 318–328. [PubMed: 18552618]

Burgoyne CF, Downs JC, Bellezza AJ, Suh JK, Hart RT, 2005. The optic nerve head as a biomechanical structure: a new paradigm for understanding the role of IOP-related stress and strain in the pathophysiology of glaucomatous optic nerve head damage. Prog Retin Eye Res 24, 39–73. [PubMed: 15555526]

Burgoyne CF, Quigley HA, Thompson HW, Vitale S, Varma R, 1995. Early changes in optic disc compliance and surface position in experimental glaucoma. Ophthalmology 102, 1800–1809. [PubMed: 9098280]

Curcio CA, Messinger JD, Sloan KR, Mitra A, McGwin G, Spaide RF, 2011. Human Chorioretinal Layer Thicknesses Measured in Macula-wide, High-Resolution Histologic Sections. Investigative Ophthalmology & Visual Science 52, 3943–3954. [PubMed: 21421869]

Downs JC, Roberts MD, Burgoyne CF, 2008. Mechanical environment of the optic nerve head in glaucoma. Optom Vis Sci 85, 425–435. [PubMed: 18521012]

Fazio MA, Clark ME, Bruno L, Girkin CA, 2018. In vivo optic nerve head mechanical response to intraocular and cerebrospinal fluid pressure: imaging protocol and quantification method. Scientific reports 8, 12639. [PubMed: 30140057]

Fazio MA, Girard MJA, Lee W, Morris JS, Burgoyne CF, Downs JC, 2019. The Relationship Between Scleral Strain Change and Differential Cumulative Intraocular Pressure Exposure in the Nonhuman Primate Chronic Ocular Hypertension Model. Investigative Ophthalmology & Visual Science 60, 4141–4150. [PubMed: 31598625]

Fazio MA, Grytz R, Morris JS, Bruno L, Gardiner SK, Girkin CA, Downs JC, 2014a. Age-related changes in human peripapillary scleral strain. Biomechanics and modeling in mechanobiology 13, 551–563. [PubMed: 23896936]

Fazio MA, Grytz R, Morris JS, Bruno L, Girkin CA, Downs JC, 2014b. Human scleral structural stiffness increases more rapidly with age in donors of African descent compared to donors of

European descent. Investigative ophthalmology & visual science 55, 7189–7198. [PubMed: 25237162]

Fazio MA, Johnstone JK, Smith B, Wang L, Girkin CA, 2016. Displacement of the Lamina Cribrosa in Response to Acute Intraocular Pressure Elevation in Normal Individuals of African and European Descent. Invest Ophthalmol Vis Sci 57, 3331–3339. [PubMed: 27367500]

Fortune B, Reynaud J, Wang L, Burgoyne CF, 2013. Does optic nerve head surface topography change prior to loss of retinal nerve fiber layer thickness: a test of the site of injury hypothesis in experimental glaucoma. PloS one 8, e77831. [PubMed: 24204989]

Girard MJ, Strouthidis NG, Ethier CR, Mari JM, 2011. Shadow removal and contrast enhancement in optical coherence tomography images of the human optic nerve head. Invest Ophthalmol Vis Sci 52, 7738–7748. [PubMed: 21551412]

Girard MJ, Tun TA, Husain R, Acharyya S, Haaland BA, Wei X, Mari JM, Perera SA, Baskaran M, Aung T, Strouthidis NG, 2015a. Lamina cribrosa visibility using optical coherence tomography: comparison of devices and effects of image enhancement techniques. Invest Ophthalmol Vis Sci 56, 865–874. [PubMed: 25593025]

Girard MJA, Tun TA, Husain R, Acharyya S, Haaland BA, Wei X, Mari JM, Perera SA, Baskaran M, Aung T, Strouthidis NG, 2015b. Lamina Cribrosa Visibility Using Optical Coherence Tomography: Comparison of Devices and Effects of Image Enhancement Techniques. Investigative Ophthalmology & Visual Science 56, 865–874. [PubMed: 25593025]

Girkin CA, Fazio MA, Bowd C, Medeiros FA, Weinreb RN, Liebmann JM, Proudfoot J, Zangwill LM, Belghith A, 2019. Racial Differences in the Association of Anterior Lamina Cribrosa Surface Depth and Glaucoma Severity in the African Descent and Glaucoma Evaluation Study (ADAGES). Investigative ophthalmology & visual science 60, 4496–4502. [PubMed: 31661550]

Girkin CA, Fazio MA, Yang H, Reynaud J, Burgoyne CF, Smith B, Wang L, Downs JC, 2017a. Variation in the three-dimensional histomorphometry of the normal human optic nerve head with age and race: lamina cribrosa and peripapillary scleral thickness and position. Investigative ophthalmology & visual science 58, 3759–3769. [PubMed: 28738420]

Girkin CA, Fazio MA, Yang H, Reynaud J, Burgoyne CF, Smith B, Wang L, Downs JC, 2017b. Variation in the Three-Dimensional Histomorphometry of the Normal Human Optic Nerve Head With Age and Race: Lamina Cribrosa and Peripapillary Scleral Thickness and Position. Invest Ophthalmol Vis Sci 58, 3759–3769. [PubMed: 28738420]

Girkin CA, Fazio MA, Yang H, Reynaud J, Burgoyne CF, Smith B, Wang L, Downs JC, 2017c. Variation in the Three-Dimensional Histomorphometry of the Normal Human Optic Nerve Head With Age and Race: Lamina Cribrosa and Peripapillary Scleral Thickness and PositionAge-and Race-Related Differences In Normal Human ONH. Investigative Ophthalmology & Visual Science 58, 3759–3769. [PubMed: 28738420]

Grytz R, Fazio MA, Girard MJA, Libertiaux V, Bruno L, Gardiner S, Girkin CA, Downs JC, 2014a. Material properties of the posterior human sclera. Journal of the mechanical behavior of biomedical materials 29, 602–617. [PubMed: 23684352]

Grytz R, Fazio MA, Libertiaux V, Bruno L, Gardiner S, Girkin CA, Downs JC, 2014b. Age- and race-related differences in human scleral material properties. Investigative ophthalmology & visual science 55, 8163–8172. [PubMed: 25389203]

Grytz R, Fuchs P, El Hamdaoui M, McNabb RP, Kuo AN, Samuels BC, 2020a. Empirical Distortion Correction for Posterior Segment SD-OCT Images in Small Animals. Investigative Ophthalmology & Visual Science 61, 4778–4778.

Grytz R, Yang H, Hua Y, Samuels BC, Sigal IA, 2020b. Connective tissue remodeling in myopia and its potential role in increasing risk of glaucoma. Current Opinion in Biomedical Engineering 15, 40–50. [PubMed: 32211567]

Johnstone J, Fazio M, Rojananuangnit K, Smith B, Clark M, Downs C, Owsley C, Girard MJ, Mari JM, Girkin CA, 2014. Variation of the axial location of Bruch's membrane opening with age, choroidal thickness, and race. Invest Ophthalmol Vis Sci 55, 2004–2009. [PubMed: 24595390]

Kim YW, Jeoung JW, Kim YK, Park KH, 2017. Clinical Implications of In Vivo Lamina Cribrosa Imaging in Glaucoma. Journal of Glaucoma 26.

Lee SH, Kim T-W, Lee EJ, Girard MJA, Mari JM, 2017. Diagnostic Power of Lamina Cribrosa Depth and Curvature in Glaucoma. Investigative Ophthalmology & Visual Science 58, 755–762. [PubMed: 28146240]

Mari JM, Strouthidis NG, Park SC, Girard MJ, 2013. Enhancement of lamina cribrosa visibility in optical coherence tomography images using adaptive compensation. Invest Ophthalmol Vis Sci 54, 2238–2247. [PubMed: 23449723]

Rhodes LA, Huisingh C, Johnstone J, Fazio M, Smith B, Clark M, Downs JC, Owsley C, Girard MJ, Mari JM, Girkin C, 2014. Variation of laminar depth in normal eyes with age and race. Invest Ophthalmol Vis Sci 55, 8123–8133. [PubMed: 25414182]

Rhodes LA, Huisingh C, Johnstone J, Fazio MA, Smith B, Wang L, Clark M, Downs JC, Owsley C, Girard MJ, Mari JM, Girkin CA, 2015. Peripapillary choroidal thickness variation with age and race in normal eyes. Invest Ophthalmol Vis Sci 56, 1872–1879. [PubMed: 25711640]

Rosenthal J, Mangal V, Walker D, Bennett M, Mohun TJ, Lo CW, 2004. Rapid high resolution three dimensional reconstruction of embryos with episcopic fluorescence image capture. Birth Defects Res C Embryo Today 72, 213–223. [PubMed: 15495188]

Sedgwick P, 2013. Limits of agreement (Bland-Altman method). BMJ : British Medical Journal 346, f1630. [PubMed: 23502707]

Sharma S, Tun TA, Baskaran M, Atalay E, Thakku SG, Liang Z, Milea D, Strouthidis NG, Aung T, Girard MJ, 2018. Effect of acute intraocular pressure elevation on the minimum rim width in normal, ocular hypertensive and glaucoma eyes. Br J Ophthalmol 102, 131–135. [PubMed: 28490427]

Sigal I, Flanagan J, Ethier C, 2005. Factors influencing optic nerve head biomechanics, Exp Eye Res, pp. 4189–4199.

Sigal IA, Grimm JL, Jan NJ, Reid K, Minckler DS, Brown DJ, 2014. Eye-specific IOP-induced displacements and deformations of human lamina cribrosa. Invest Ophthalmol Vis Sci 55, 1–15. [PubMed: 24334450]

Spaide RF, Curcio CA, 2011. Anatomical correlates to the bands seen in the outer retina by optical coherence tomography: literature review and model. Retina 31, 1609–1619. [PubMed: 21844839]

Spaide RF, Koizumi H, Pozzoni MC, 2008. Enhanced depth imaging spectral-domain optical coherence tomography. Am J Ophthalmol 146, 496–500. [PubMed: 18639219]

Staurenghi G, Sadda S, Chakravarthy U, Spaide RF, International Nomenclature for Optical Coherence Tomography, P., 2014. Proposed lexicon for anatomic landmarks in normal posterior segment spectral-domain optical coherence tomography: the IN*OCT consensus. Ophthalmology 121, 1572–1578. [PubMed: 24755005]

Thakku SG, Tham Y-C, Baskaran M, Mari J-M, Strouthidis NG, Aung T, Cheng C-Y, Girard MJA, 2015. A Global Shape Index to Characterize Anterior Lamina Cribrosa Morphology and Its Determinants in Healthy Indian Eyes. Investigative Ophthalmology & Visual Science 56, 3604–3614. [PubMed: 26047047]

Tran H, Wallace J, Zhu Z, Lucy KA, Voorhees AP, Schmitt SE, Bilonick RA, Schuman JS, Smith MA, Wollstein G, Sigal IA, 2018. Seeing the Hidden Lamina: Effects of Exsanguination on the Optic Nerve Head. Investigative Ophthalmology & Visual Science 59, 2564–2575. [PubMed: 29847664]

Vermeer KA, Mo J, Weda JJ, Lemij HG, de Boer JF, 2013. Depth-resolved model-based reconstruction of attenuation coefficients in optical coherence tomography. Biomedical optics express 5, 322–337. [PubMed: 24466497]

Wang YX, Yang H, Luo H, Hong SW, Gardiner SK, Jeoung JW, Caprioli J, Demirel S, Girkin CA, Liebmann JM, Mardin CY, Quigley HA, Scheuerle AF, Chauhan BC, Burgoyne CF, 2019. Optical Coherence Tomography (OCT) Anterior Scleral Canal Opening (ASCO) Tilt and Rotation relative to Bruch's Membrane Opening (BMO) and Peripapillary Scleral Bowing (PSB) in Healthy Eyes. Investigative Ophthalmology & Visual Science 60, 5516–5516.

Weninger WJ, Mohun T, 2002. Phenotyping transgenic embryos: a rapid 3-D screening method based on episcopic fluorescence image capturing. Nat Genet 30, 59–65. [PubMed: 11743576]

Yang H, Downs JC, Girkin C, Sakata L, Bellezza A, Thompson H, Burgoyne CF, 2007. 3-D Histomorphometry of the Normal and Early Glaucomatous Monkey Optic Nerve Head: Lamina

Cribrosa and Peripapillary Scleral Position and Thickness. Investigative Ophthalmology & Visual Science 48, 4597–4607. [PubMed: 17898283]

Yang H, Luo H, Gardiner SK, Hardin C, Sharpe GP, Caprioli J, Demirel S, Girkin CA, Liebmann JM, Mardin CY, Quigley HA, Scheuerle AF, Fortune B, Chauhan BC, Burgoyne CF, 2019. Factors Influencing Optical Coherence Tomography Peripapillary Choroidal Thickness: A Multicenter Study. Investigative Ophthalmology & Visual Science 60, 795–806. [PubMed: 30811523]

Zhang D, 2017. A Coefficient of Determination for Generalized Linear Models. The American Statistician 71, 310–316.

Highlights:

- This study presents the first histologic validation of the ONH tissues imaged by OCT.
- OCT imaging of the deep optic nerve tissues show promising correspondence to ex vivo histology imaging.
- On average, only 31% of the anterior laminar surface was visible in vivo by OCT imaging compared to histology.
- On average, anterior laminar surface depth was 30% higher in vivo compared to histology.

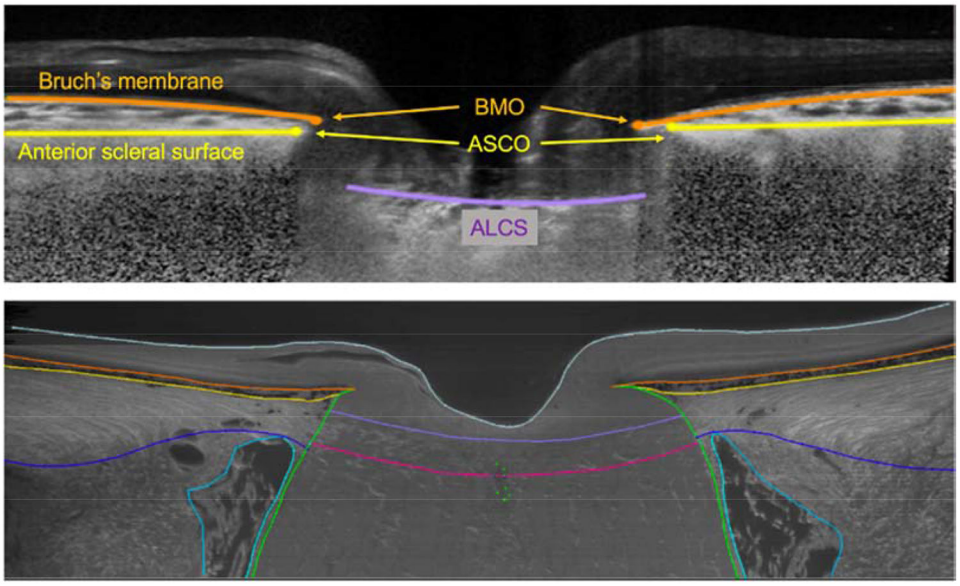

Figure 1.

Custom software to delineate ONH anatomy of the same brain-dead organ donor eye in both in vivo (before organ recovery by optical coherence tomography; OCT) and ex vivo conditions (after 3D reconstruction with episcopic autofluorescence imaging). In the OCT B-scan (upper plot), The Bruch's membrane and opening (BMO) are marked in orange; anterior scleral surface and opening (ASCO) is marked in yellow; anterior lamina cribrosa surface (ALCS) is marked in fuchsia. In the digital section of the 3D histology reconstruction representing the same location in the ONH depicted in the OCT B-scan above. In the histology, additional landmarks of the retina are visible and delineated: the posterior lamina cribrosa surface is marked in red; pia mater is marked in green; posterior scleral surface in blue; internal surface of the dura mater in cyan. Internal limiting membrane marked in gray.

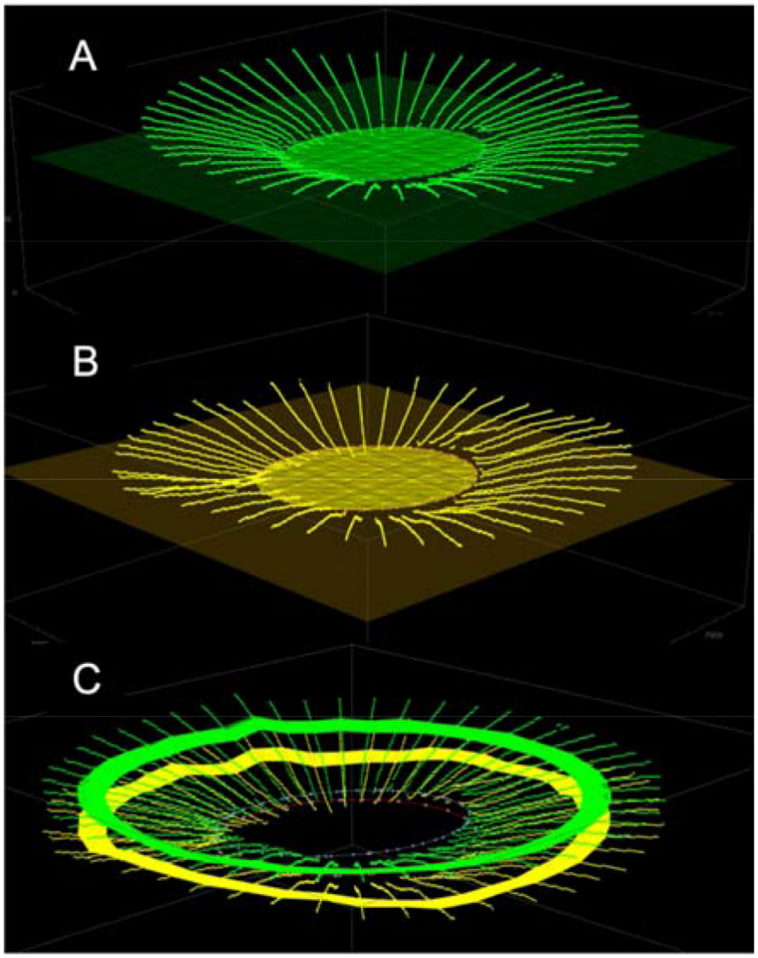

Fig. 2.

Representation of the three-dimensional fitting of the Bruch's membrane (BM) (in green; plot A) and anterior scleral points (in yellow; plot B). Plot C: BM and anterior sclera points belonging to a 250-μm-wide anulus radially distant 1500μm from the optic nerve head center was used to compute BM- and sclera-based reference planes and choroidal thickness.

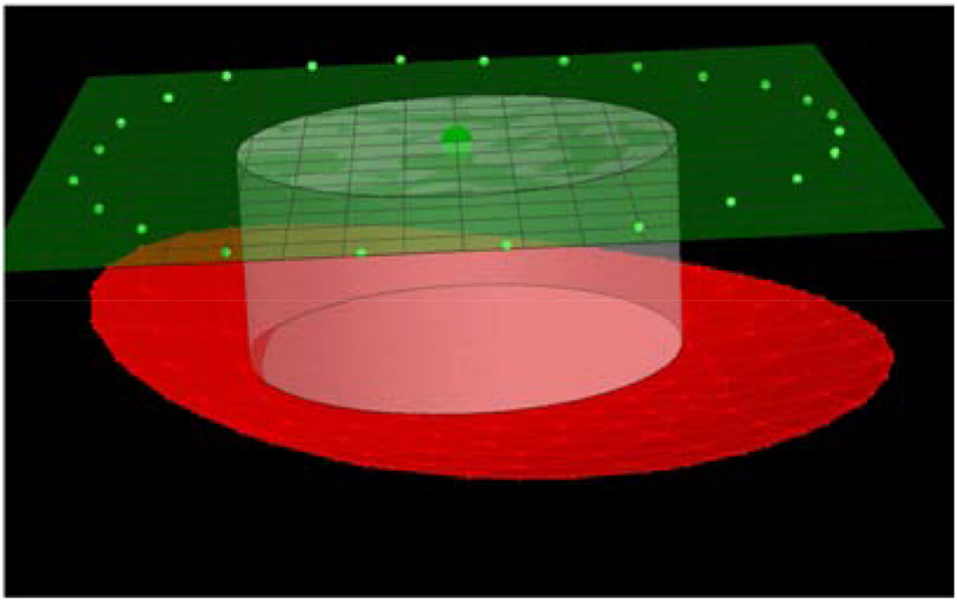

Fig. 3.

In red, representation of the three-dimensional paraboloid fitting of the anterior lamina cribrosa surface (ALCS). In white, 500-μm-radius cylinder perpendicular to the BMO reference plane (in green), and passing for the BMO centroid (dark green). The intersection between the cylinder and ALCS defined the central portion of the ALCS for which ALCS depth is computed. Depth was computed as the average distance between the central ALCS and the BMO reference plane.

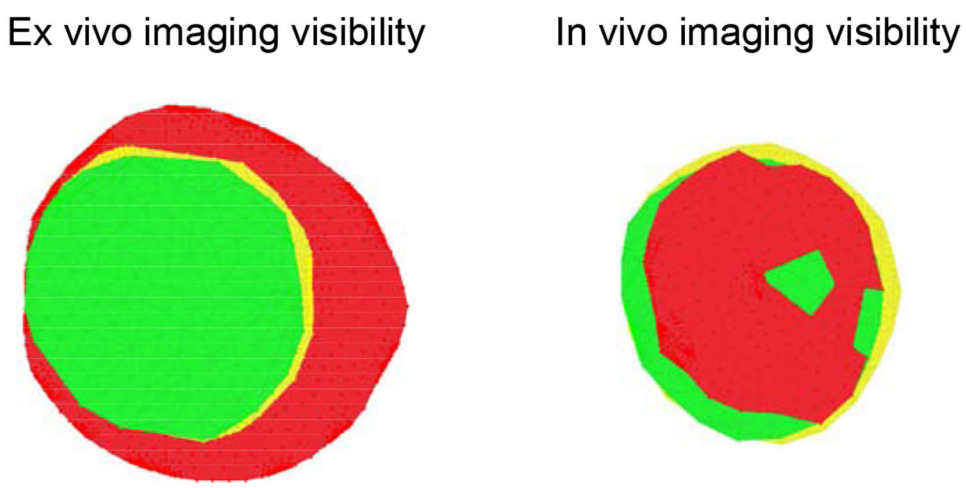

Fig. 4.

En face views of the visible anterior lamina cribrosa surface (ALCS, in red) delineation points, anterior scleral canal opening (ASCO, in yellow) area, and Bruch's membrane opening (BMO, in green) area. Left plot: Visibility of these regions in the ex vivo episcopic autofluorescence histology images. Right plot: Visibility of these regions in the vivo optical coherence tomography images. Notice the much smaller visibility of ALCS in vivo.

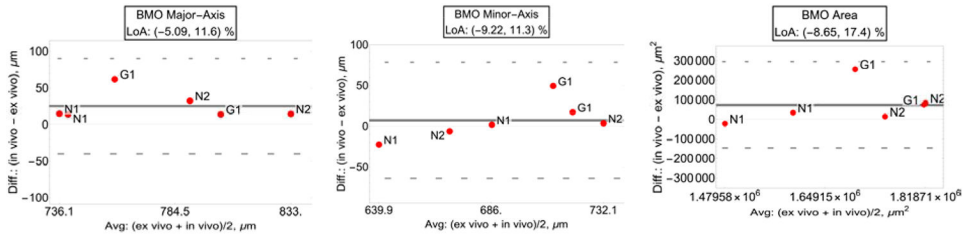

Fig. 5.

Bland-Altman plots with limit of agreement (LoA) of BMO major axis (left plot), BMO minor axis (center plot), and BMO area (right plot). (“N”: normal eyes; “G”: glaucoma eyes.)

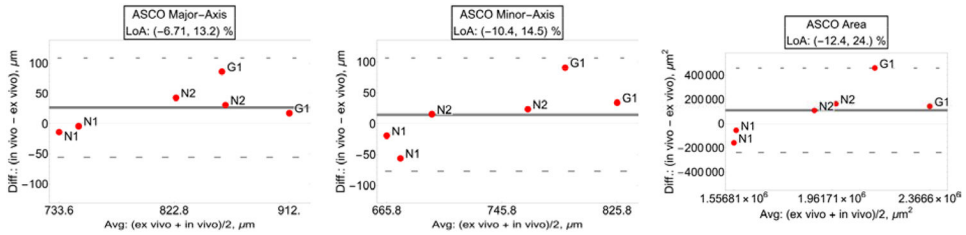

Fig. 6.

Bland-Altman plots with limit of agreement (LoA) of ASCO major axis (left plot), ASCO minor axis (center plot) and ASCO area (right plot).

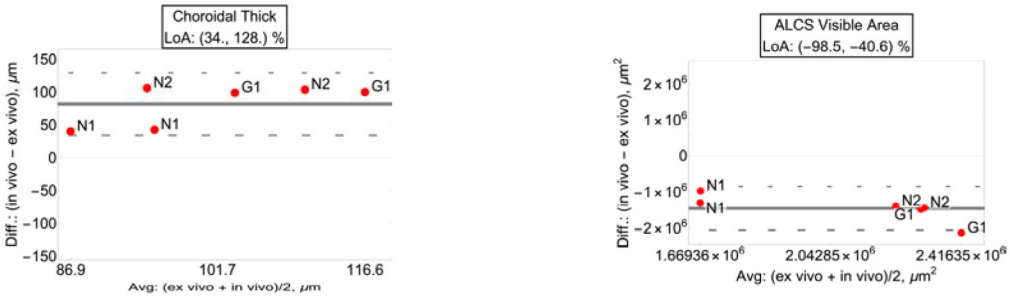

Fig. 7.

Left plot: Bland-Altman and limit of agreement (LoA) for choroidal thickness showed a thicker choroid in the in vivo measures. Right plot: anterior lamina cribrosa surface (ALCS) visibility area LoA showed a large reduction of visibility in the in vivo measures compared to ex vivo.

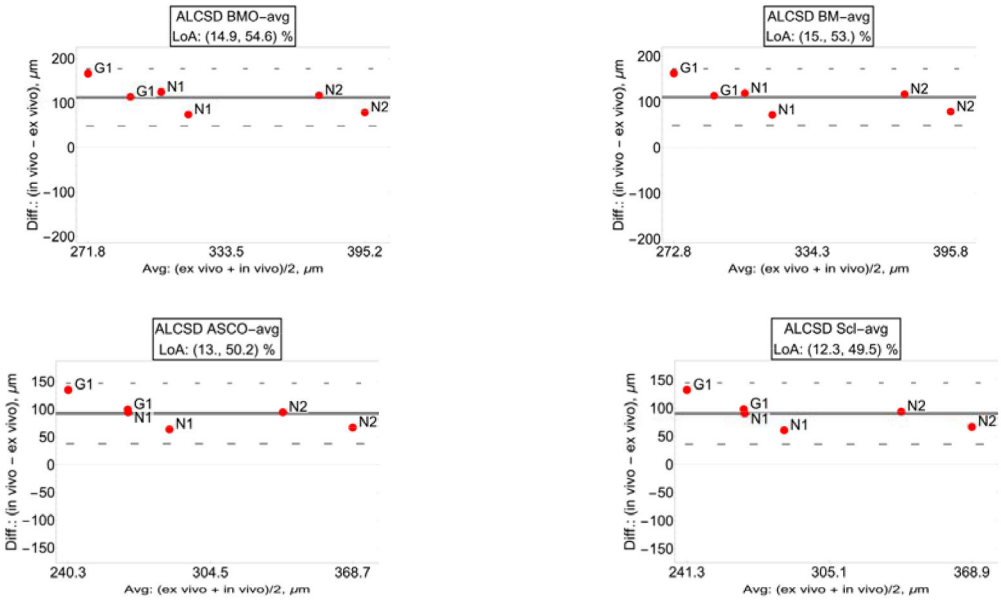

Fig. 8.

Bland-Altman plots with limit of agreement (LoA) of the ALCS distance from: the BMO reference plane (top-left); the BM reference plane (top-right); ASCO reference plane (bottom-left); sclera reference plane (bottom-right).

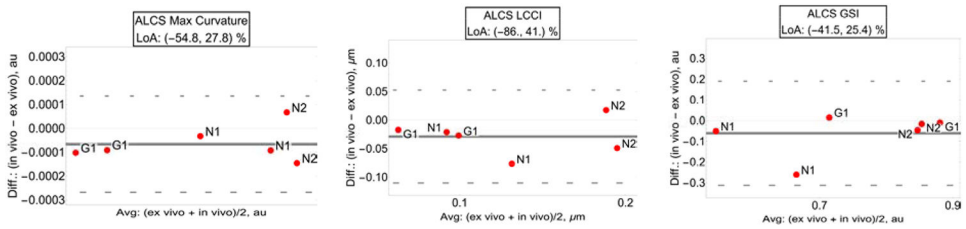

Fig. 9.

Bland-Altman plots with limit of agreement (LoA) of BMO maximum curvature (left plot), minimum curvature (center plot) and global shape index (right plot).

Table 1.

Correlation analysis of the in vivo and ex vivo metrics along with means and limits of agreement (LoA) of the relative difference between in vivo and ex vivo metrics for all parameters. The first p-value tests whether the in vivo and ex vivo metrics are correlated. The second p-value tests whether the LoA includes zero, i.e. a significant p-value indicates a non-zero offset between the in vivo and ex vivo values.

Morphological parameters		Correlation		Relative difference		
		R^2	p-value	Estimated Mean	LoA	p-value
BMO	Major axis	0.779	<0.001	3.28 %	[−5.09, 11.6] %	0.026
	Minor axis	0.737	<0.001	0.959 %	[−9.22, 11.3] %	0.53
	Area	0.62	<0.001	4.23 %	[−8.65, 17.4] %	0.13
ASCO	Major axis	0.834	<0.001	3.09 %	[−6.71, 13.2] %	0.14
	Minor axis	0.762	<0.001	1.64 %	[−10.4, 14.5] %	0.58
	Area	0.798	<0.001	4.72 %	[−12.4, 24.0.] %	0.33
Choroid	Thickness	0.201	0.036	79.9 %	[34.0, 128.0] %	<0.001
ALCS visibility	Visible area	0.454	<0.001	−69.2 %	[−98.5, -40.6] %	<0.001
ALCS depth	BMO reference plane	0.716	<0.001	36.2 %	[14.9, 54.6] %	0.0019
	BM reference plane	0.721	<0.001	35.4 %	[15.0, 53.0] %	0.0018
	ASCO reference plane	0.843	<0.001	33.1 %	[13.0, 50.2] %	0.0019
	Sclera reference plane	0.83	<0.001	32.3 %	[12.3, 49.5] %	0.0019
ALCS shape	Max curvature	0.835	<0.001	−17.1 %	[−54.8, 27.8] %	0.064
	LCCI	0.706	<0.001	−25.2 %	[−86.0, 41.0] %	0.035
	GSI	0.596	<0.001	−9.01 %	[−41.5, 25.4] %	0.21